

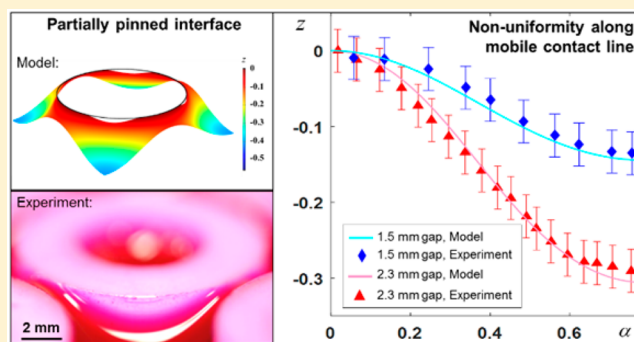
Coexistence of Pinning and Moving on a Contact Line

Zhengmao Lu,[†] Daniel J. Preston,[†] Dion S. Antao, Yangying Zhu, and Evelyn N. Wang*

Department of Mechanical Engineering, Massachusetts Institute of Technology, Cambridge, Massachusetts 02139, United States

Supporting Information

ABSTRACT: Textured surfaces are instrumental in water repellency or fluid wicking applications, where the pinning and depinning of the liquid–gas interface plays an important role. Previous work showed that a contact line can exhibit nonuniform behavior due to heterogeneities in surface chemistry or roughness. We demonstrate that such nonuniformities can be achieved even without varying the local energy barrier. Around a cylindrical pillar, an interface can reside in an intermediate state where segments of the contact line are pinned to the pillar top while the rest of the contact line moves along the sidewall. This partially pinned mode is due to the global nonaxisymmetric pattern of the surface features and exists for all textured surfaces, especially when superhydrophobic surfaces are about to be flooded or when capillary wicks are close to dryout.



INTRODUCTION

Rough, structured surfaces are used to manipulate the liquid–gas interface primarily for two purposes: fluid repellency^{1–3} for self-cleaning,^{4,5} water harvesting,⁶ anti-icing,⁷ antifouling,⁸ and enhancing condensation,^{9–12} and capillary wicking for thermal management,^{13–16} microfluidics,^{17–19} and fluid separation.²⁰ In both cases, liquid and gas are separated by a capillary surface²¹ which self-regulates its shape in response to the interfacial pressure difference. Prior work has recognized the importance of the capillary surface evolution and the contact line pinning/depinning in these applications, where the contact line has been commonly considered to be either fully pinned or mobile.^{22–32}

We show through experiments and modeling a hybrid wetting state during which contact line pinning and motion coexist. Similar coexistence behavior has been reported in literature for a sessile drop placed on a substrate with heterogeneities in surface chemistry or roughness.^{33–37} In these cases, the local energy barrier, which governs the pinning/depinning or contact angle hysteresis, in general, is manipulated along the contact line. However, we demonstrate that the contact line can exhibit nonuniform behavior simply due to the global nonaxisymmetric pattern of the surface features, without variation in the local energy barrier. Because this non-axisymmetry is present for all textured surfaces, the current work is relevant for all of the fluid repellency and wicking applications described above. In this study, with a regular pillar array system,^{38–44} as we varied the interfacial pressure difference, we observed the fully pinned mode of the contact line in Figure 1a,b and the fully mobile mode in Figure 1e,f; additionally, between these two modes, we show the existence of the previously unexplored partially pinned mode in the absence of local energy barrier variation in Figure 1c,d.

MODEL FORMULATION

To understand the interface behavior during the transition from a pinned to mobile contact line, we established a model framework based on first-principles, where we examined the capillary surface in a unit cell of a square-patterned cylindrical pillar array, representative of structures on engineered surfaces. We denote the pillar radius as r , center-to-center spacing as L , and gap between pillars as $s = L - 2r$ and establish a Cartesian coordinate system at the center of one of the pillars (Figure 2a,b). The shape of the interface is described by $z = f(x, y)$. Because of symmetry, we restrict the problem domain to one-eighth of the unit cell and consequently apply symmetry boundary conditions on boundaries 1, 2, and 3 in Figure 2c. By the pressure balance across the interface,

$$\Delta P_0 + \Delta \rho g z = 2\sigma \kappa \quad (1)$$

where ΔP_0 is the interfacial pressure difference from phase 2 to phase 1 in Figure 2a evaluated at the highest point of the interface ($z = 0$), σ is the surface tension, κ is the interface mean curvature, $\Delta \rho$ is the density difference from phase 1 to phase 2, and g is the gravitational constant. Normalizing both sides of eq 1 to the characteristic capillary pressure σ/r , we have

$$\frac{\Delta P_0}{\sigma/r} + \text{Bo} \cdot \frac{z}{r} = 2\kappa r \quad (2)$$

where $\text{Bo} = \Delta \rho g r^2 / \sigma$ is the Bond number²¹ of the system. From this dimensionless equation, it is clear that the system's behavior is dominated by Bo and the ratio between the

Received: June 17, 2017

Revised: August 13, 2017

Published: August 17, 2017

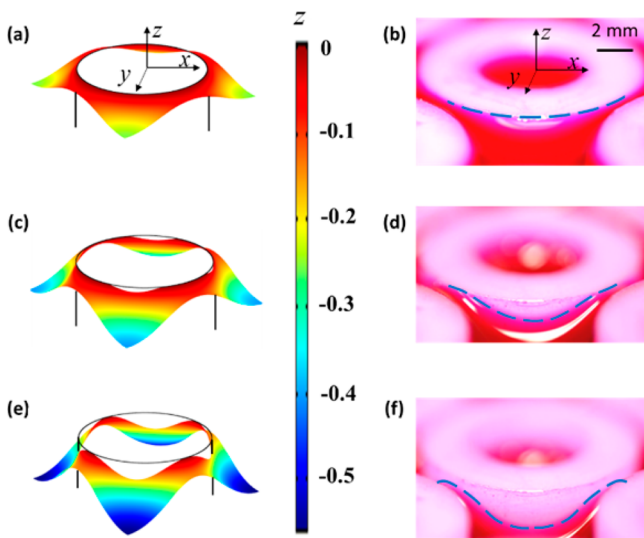


Figure 1. Model solution and experimental observation of the capillary surface around a cylindrical pillar in a square array: (a,b) Regime (I) fully pinned mode; (c,d) Regime (II) partially pinned mode; and (e,f) fully mobile mode. The colors in panels a, c, and e represent the z coordinates of the capillary surface. The blue dashed lines in panels b, d, and f indicate the contact line position. The major difference between the model (a,c,e) and the experiment (b,d,f) is the Bo. The former assumes $Bo \ll 1$, while the latter corresponds to $Bo = 6.3$. Nevertheless, the same three regime behaviors were observed in both the model and the experiment. Noting that gravity only tends to flatten the interface, the experimental observations qualitatively support the modeling results.

interface geometry and pillar radius. Note that when $Bo \gg 1$, gravity dominates, resulting in a flat interface as the right-hand side of eq 2 becomes negligible, so any nonuniform behavior of the contact line should be caused by capillarity. When $Bo \ll 1$, κ remains constant in a unit cell as the gravitational term diminishes, reducing eq 2 to the Young–Laplace equation. Applying concepts from differential geometry,⁴⁵ κ , which is positive when phase 2 curves into phase 1, can be determined

from the outward-pointing unit normal vector of the interface $\hat{n} = \nabla f / \|\nabla f\|$ (Figure 2a)

$$\nabla \cdot \hat{n} = 2\kappa \quad (3)$$

Applying the divergence theorem for the vector field \hat{n} , we have

$$\iint \nabla \cdot \hat{n} ds = \oint_{1,2,3,4} \hat{n} \cdot \hat{n}_b dl \quad (4)$$

The left-hand side is the gradient of \hat{n} integrated over the problem domain in Figure 2c and the right-hand side is the dot product between \hat{n} and \hat{n}_b integrated over boundaries 1, 2, 3, and 4 in Figure 2c, where \hat{n}_b is the boundary unit normal vector pointing outward. Because of the symmetry, $\hat{n} \cdot \hat{n}_b = 0$ on boundaries 1, 2, and 3. On boundary 4, $\hat{n}_b = \hat{n}_4 = (-x, -y, 0)$. Combining eqs 3 and 4, we have

$$\iint 2\kappa ds = \int_4 \hat{n} \cdot \hat{n}_4 dl \quad (5)$$

Equation 3 is a second-order partial differential equation that governs the shape of the capillary surface $z = f(x, y)$. With proper boundary conditions specified at boundaries 1, 2, 3, and 4, it can be solved by the finite element method where we applied the sparse object-oriented linear equations solver⁴⁶ and used free triangular meshing with 40,508 domain elements and 2124 boundary elements while the relative tolerance for convergence was set to be 10^{-6} . (See Supporting Information, Section I for a comparison between the present work and the Surface Evolver⁴⁷ approach.)

MODELING RESULTS AND DISCUSSION

We set $r = 1$ to normalize the pillar array dimensions to its radius and $L = 2.5$ as a reference geometry. When the contact line is fully pinned at the top of the pillar, we have a Dirichlet condition ($z = 0$) on boundary 4, which enables us to solve eqs 2 and 3 for a given κ . For example, setting $\kappa = 0.6$, we plot the shape of the capillary surface around one pillar in Figure 1a. We evaluate the apparent contact angle θ as the angle between \hat{n} and \hat{n}_4 with $\cos \theta = \hat{n} \cdot \hat{n}_4$. When the contact line is fully mobile along the sidewall, the boundary condition on the contact line is determined by $\theta = \theta_r$, where θ_r is the receding contact angle

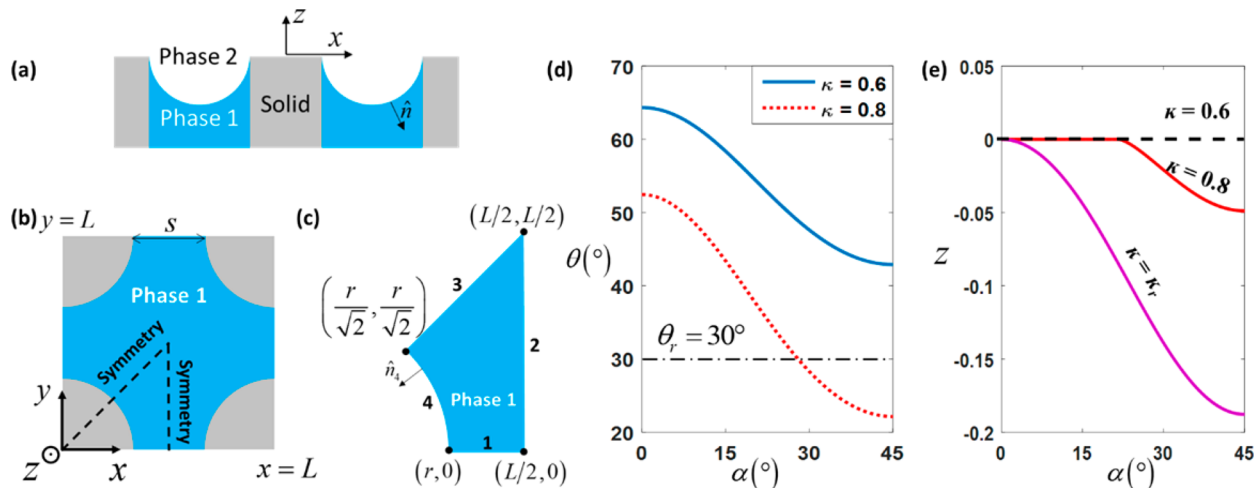


Figure 2. (a) Schematic side view of capillary surface formed in pillar arrays. (b) Top view of a unit cell of a square-patterned cylindrical pillar array. (c) Problem domain for solving the capillary surface: Only 1/8 of the interface in the unit cell is simulated due to symmetry. (d) Contact angle θ plotted against polar angle α for $L = 2.5$, $\kappa = 0.6$ (blue solid line) and $\kappa = 0.8$ (red dotted line) in the fully pinned mode. (e) Contact line location as a function of polar angle α for $\kappa = 0.6$, $\kappa = 0.8$, and $\kappa = \kappa_r$ when $\theta_r = 30^\circ$.

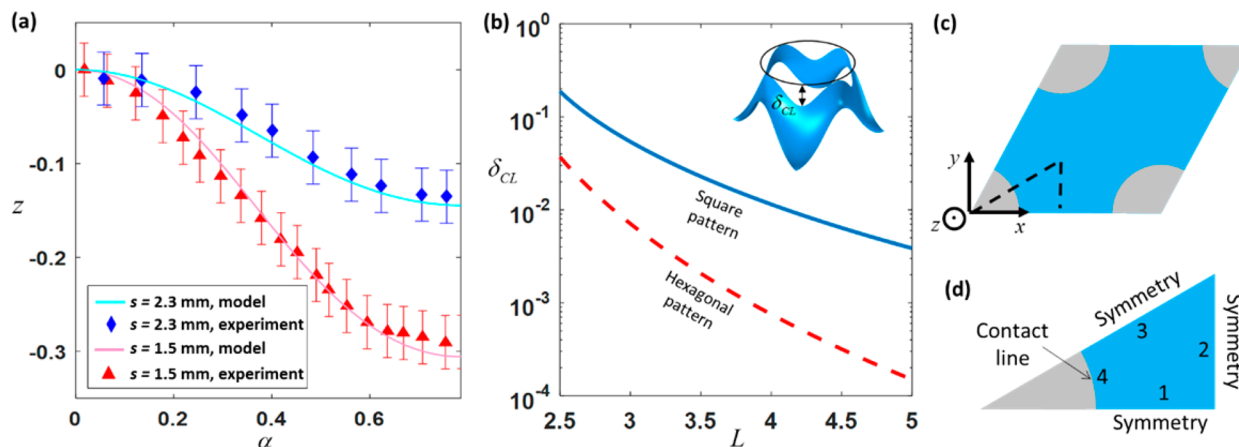


Figure 3. (a) Model validation using the contact line location in the fully mobile mode for two sample pillar arrays ($Bo = 6.3$): the light-blue curve and blue diamond symbols represent the model prediction and experimental data, respectively, for a square array of 12.7 mm diameter pillars with 2.3 mm gap between pillars; the light-red curve and red triangle symbols represent the model prediction and experimental data, respectively, for a square array of 12.7 mm diameter pillars with 1.5 mm gap between pillars. (b) Variation in the contact line location (δ_{CL}) as a function of L for square-patterned and hexagonal-patterned pillar arrays for $Bo \ll 1$. (c) Top view of a unit cell of a hexagonal-patterned pillar array. (d) Problem domain with boundary conditions for predicting the capillary surface in a hexagonal-patterned pillar array.

of phase 1 (or the advancing contact angle of phase 2) and the capillary surface generates the maximum mean curvature $\kappa = \kappa_r$. The divergence theorem in eq 5 then reduced to

$$2\kappa_r \frac{(L^2 - \pi r^2)}{8} = \frac{\pi r}{4} \cos \theta_r \quad (6)$$

For example, setting $\theta_r = 30^\circ$, we obtain $\kappa_r \approx 0.875$ and plot the capillary surface in Figure 1e. Between the Regime (I) fully pinned mode and the Regime (III) fully mobile mode, there exists a partially pinned mode (Regime (II)) where part of the contact line depins and the rest remains pinned. For instance, with $L = 2.5$, $\kappa = 0.8$, and $\theta_r = 30^\circ$, we plot the $z = f(x, y)$ solution in Figure 1c for the partially pinned regime. In general, to determine whether the capillary surface falls into the partially pinned regime given a $\kappa < \kappa_r$, first $z = f(x, y)$ is solved assuming the fully pinned mode and θ is plotted against the polar angle $\alpha = \arctan(y/x)$ along the contact line. The capillary surface stays in the fully pinned mode if and only if $\theta \geq \theta_r$ at every location of the contact line. In Figure 2d, when $\theta_r = 30^\circ$ and $\kappa = 0.6$, $\theta \geq \theta_r$ for any α (Regime (I)). However, when $\kappa = 0.8$, we observe that $\theta < \theta_r$ for part of the contact line, which indicates that the contact line partially depins and transitions into the partially pinned mode (Regime (II)). Then, we need to relax the boundary condition on the contact line to be either $z = 0$ or $\theta = \theta_r$ while enforcing the continuity in z and θ . In Figure 2e, the contact line location is plotted against α ($0 \leq \alpha \leq 45^\circ$) for all three modes ($\kappa = 0.6$ fully pinned, $\kappa = 0.8$ partially pinned, and $\kappa = \kappa_r$ fully mobile regimes), which elaborates on the contact line behaviors as κ or equivalently ΔP_0 increases. The evolution of the capillary surface is important for determining the flooding criteria on superhydrophobic surfaces and the thermal-fluidic resistance in thermal management and microfluidic devices based on capillary wicks (see Supporting Information, Section II). We note that the model that we developed here does not necessarily capture the dynamics of the contact line. For example, the depinning event at one point can instantly change the curvature of the capillary surface in its surroundings.⁴⁸ Therefore, the evolution of the interface is depicted by this model in only a quasi-static way.

In all three regimes, there is nonuniformity in either θ or z on the contact line. For example, in the fully pinned mode in Figure 2d, θ is smaller where α is larger. As ΔP_0 increases, the interface becomes more curved to generate a larger capillary pressure and θ decreases down to the limit of θ_r . Consequently, where α is larger, θ will approach θ_r first. As ΔP_0 is increased further, the depinning of the contact line starts from the location where $\alpha = 45^\circ$, moving in the direction of decreasing α . As a result, when the contact line fully depins, it is at a lower location for larger α , as indicated in Figure 2e. We attribute this nonuniformity to the nonaxisymmetry of the square pattern of the pillar array even though the cylindrical pillar itself is axisymmetric. Because of this mismatch, not every location on the contact line transitions from pinned to mobile at the same time, which is the reason that the partially pinned regime exists. In general, Regime (II) exists for any surface that is not axisymmetric.

EXPERIMENTAL RESULTS AND DISCUSSION

To verify the findings of our model, we created two square-patterned cylindrical pillar arrays using nylon pillars, 12.7 mm in diameter with gap between pillars $s = 1.5$ and 2.3 mm, respectively. We used a solution of Rhodamine B in water (2.09 mM) as the working fluid. The surface tension was determined to be 62 mN/m using the pendant drop method,⁴⁹ which agrees with literature data.⁵⁰ On this length scale, the gravitational term in eq 2 becomes comparable to the capillary term as $Bo = 6.3$. The quasi-static receding contact angle of the solution on the pillar surface is measured to be $\theta_r = 10^\circ$ with the dynamic sessile drop method. During the experiment, we slowly pulled out the liquid from the pillar array (with a Capillary number for the receding fluid of $Ca \approx 7 \times 10^{-7}$) and observed that pinning and depinning occurred on the pillar surface, as shown in Figure 1b,d,f. Noting that gravity only tends to flatten the interface, these observations qualitatively support our modeling results for the $Bo \ll 1$ case. To quantitatively validate our model, we solved eqs 2 and 3 with $Bo = 6.3$ and compared its prediction to the contact line location obtained from the fully mobile mode (Figure 1f) via image processing (see Supporting Information, Section III).

Figure 3a shows good agreement between the model and experiment, where the only model inputs are Bo , θ_v , and the pillar array geometries. In fact, we also observed the same contact line behavior on microfabricated silicon micropillar arrays ($Bo < 0.01$) using an environmental scanning electron microscope with water as the working fluid⁴⁴ (see Supporting Information, Section IV). We also note that the pillar surface in practice is not perfectly smooth and can induce local pinning. However, this only influences the contact line behavior on the length scale of the surface roughness, and the nonuniform receding that we observed on the length scale of the pillar radius is caused by the nonaxisymmetry of the surface structure pattern.

Figure 3a shows that the z coordinates of the contact line vary around the pillar in Regime (III). This is because the contact line does not depin simultaneously in Regime (II), which again originates from the nonaxisymmetry of the surface structure pattern. We evaluated δ_{CL} , the difference between the highest and the lowest points on the contact line (for $Bo \ll 1$), to quantify this nonaxisymmetric effect. In Figure 3b, δ_{CL} is plotted as a function of L for square-patterned pillar arrays (blue solid line). Note that the interaction between neighboring cells is through the non-axisymmetric periodic boundaries disturbing the capillary surface around the pillar. As L increases and the distance between the pillar and the periodic boundary is larger, this interaction becomes weaker and δ_{CL} diminishes. In the extreme case where $L \rightarrow \infty$, it corresponds to the constant mean curvature problem around a single cylindrical pillar, which is by nature axisymmetric and results in $\delta_{CL} = 0$. If we replace the square pattern with a hexagonal pattern, then δ_{CL} as a function of L (red dotted line in Figure 3b) follows a similar trend. However, at the same L , δ_{CL} is smaller for the hexagonal pattern than the square pattern, as one pillar has more nearest-neighbors in the hexagonal pattern. Note that in the hexagonal pattern pillar arrays the capillary surface is still governed by eqs 2 and 3. The unit cell is given in Figure 3c and the problem domain can be reduced to one twelfth of the unit cell due to symmetry (Figure 3d). This δ_{CL} is of significance when coatings are applied to surface structures to further tune surface wettability.^{51,52} To achieve the desired effect, the coating must be of good quality down to the depth δ_{CL} to which the contact line extends.

CONCLUSIONS

This work investigated the capillary surface evolution as a function of the interfacial pressure difference and demonstrated an intermediate regime of the liquid–vapor interface, where only part of the contact line is mobile while the rest is still pinned. This intermediate regime fundamentally originates from the nonaxisymmetry of the surface structure pattern and gives rise to the extension of the contact line length when the contact line becomes fully mobile. This partially pinned mode can play an important role when the structured surface is close to dry-out in fluid wicking or when the trapped air layer is about to be flooded during fluid repellency. As the surface structures are packed closer, which generally enhances capillarity, we observe a more pronounced partially pinned mode. We anticipate that surface structures can be finely designed to tune this partially pinned mode, which is potentially useful for water-repellency, microfluidics, and phase-change heat transfer applications.

ASSOCIATED CONTENT

Supporting Information

The Supporting Information is available free of charge on the ACS Publications website at DOI: 10.1021/acs.langmuir.7b02070.

Figure S1. Volume V as a function of curvature κ evaluated using both our current method and SE, which are in excellent agreement. Figure S2. Lowest location on the interface z_{\min} and its normalized surface area A^* as a function of κ . Figure S3 Image processing on the fully receding mode to extract the contact line location. Figure S4. Cylindrical silicon pillars were microfabricated for experimental imaging of the receding contact line with an environmental scanning electron microscope (ESEM). The pillars were cooled and water vapor was condensed onto the pillars until their walls were completely wetted, corresponding to Regime (I). This time lapse, zoomed into the sidewall of one pillar, shows the subsequent receding of the contact line during evaporation of liquid water. Figure S5. Top view of a unit cell of a square pattern micropillar array with pillars of square cross-section. 2-D contour map of the interface shape in the problem domain. 3-D reconstruction of capillary surface around one pillar in a square pattern micropillar array with pillars of square cross-section. (PDF)

AUTHOR INFORMATION

Corresponding Author

*E-mail: enwang@mit.edu.

ORCID

Zhengmao Lu: 0000-0002-5938-717X

Author Contributions

[†]Z.L. and D.J.P. contributed equally to this work

Notes

The authors declare no competing financial interest.

ACKNOWLEDGMENTS

We gratefully acknowledge funding support from the Air Force Office of Scientific Research with Dr. Ali Sayir as program manager and the Office of Naval Research (ONR) with Dr. Mark Spector as program manager. D.J.P. acknowledges funding received by the National Science Foundation Graduate Research Fellowship under Grant No. 1122374. Any opinion, findings, conclusions, or recommendations expressed in this material are those of the authors(s) and do not necessarily reflect the views of the National Science Foundation. This work was performed in part at the Center for Nanoscale Systems (CNS), a member of the National Nanotechnology Infrastructure Network (NNIN), which is supported by the National Science Foundation under NSF award no. ECS-0335765. CNS is part of Harvard University.

REFERENCES

- (1) Quéré, D.; Reyssat, M. Non-adhesive lotus and other hydrophobic materials. *Philos. Trans. R. Soc., A* **2008**, 366 (1870), 1539–1556.
- (2) Yao, X.; Chen, Q.; Xu, L.; Li, Q.; Song, Y.; Gao, X.; Quéré, D.; Jiang, L. Bioinspired ribbed nanoneedles with robust superhydrophobicity. *Adv. Funct. Mater.* **2010**, 20 (4), 656–662.
- (3) Liu, T. Y.; Kim, C. J. Turning a surface superrepellent even to completely wetting liquids. *Science* **2014**, 346 (6213), 1096–1100.

- (4) Nishimoto, S.; Bhushan, B. Bioinspired self-cleaning surfaces with superhydrophobicity, superoleophobicity, and superhydrophilicity. *RSC Adv.* **2013**, *3* (3), 671–690.
- (5) Duez, C.; Ybert, C.; Clanet, C.; Bocquet, L. Making a splash with water repellency. *Nat. Phys.* **2007**, *3* (3), 180–183.
- (6) Brown, P. S.; Bhushan, B. Bioinspired materials for water supply and management: water collection, water purification and separation of water from oil. *Philos. Trans. R. Soc., A* **2016**, *374* (2073), 20160135.
- (7) Boreyko, J. B.; Collier, P. C. Delayed Frost Growth on Jumping-Drop Superhydrophobic Surfaces. *ACS Nano* **2013**, *7*, 1618.
- (8) Genzer, J.; Efimenko, K. Recent developments in superhydrophobic surfaces and their relevance to marine fouling: a review. *Biofouling* **2006**, *22* (5), 339–360.
- (9) Preston, D. J.; Miljkovic, N.; Enright, R.; Wang, E. N. Jumping Droplet Electrostatic Charging and Effect on Vapor Drag. *J. Heat Transfer* **2014**, *136*, 080909.
- (10) Boreyko, J. B.; Chen, C. H. Self-Propelled Dropwise Condensate on Superhydrophobic Surfaces. *Phys. Rev. Lett.* **2009**, *103* (18), 184501-1–184501-4.
- (11) Narhe, R.; Beysens, D. Nucleation and growth on a superhydrophobic grooved surface. *Phys. Rev. Lett.* **2004**, *93* (7), 076103.
- (12) Cavalli, A.; Preston, D. J.; Tio, E.; Martin, D. W.; Miljkovic, N.; Wang, E. N.; Blanchette, F.; Bush, J. W. M. Electrically induced drop detachment and ejection. *Phys. Fluids* **2016**, *28* (2), 022101.
- (13) Cho, H. J.; Preston, D. J.; Zhu, Y.; Wang, E. N. Nano-engineering materials for liquid–vapour phase-change heat transfer. *Nat. Rev. Mater.* **2016**, *2* (2), 16092.
- (14) Zhu, Y.; Antao, D. S.; Lu, Z.; Somasundaram, S.; Zhang, T.; Wang, E. N. Prediction and Characterization of Dry-out Heat Flux in Micropillar Wick Structures. *Langmuir* **2016**, *32* (7), 1920–1927.
- (15) Lu, Z.; Narayanan, S.; Wang, E. N. Modeling of evaporation from nanopores with nonequilibrium and nonlocal effects. *Langmuir* **2015**, *31* (36), 9817–9824.
- (16) Lu, Z.; Salamon, T. R.; Narayanan, S.; Bagnall, K. R.; Hanks, D. F.; Antao, D. S.; Barabadi, B.; Sircar, J.; Simon, M. E.; Wang, E. N. Design and Modeling of Membrane-Based Evaporative Cooling Devices for Thermal Management of High Heat Fluxes. *IEEE Trans. Compon., Packag., Manuf. Technol.* **2016**, *6* (7), 1056–1065.
- (17) Jung, S. M.; Preston, D. J.; Jung, H. Y.; Deng, Z. T.; Wang, E. N.; Kong, J. Porous Cu Nanowire Aerosponges from One-Step Assembly and their Applications in Heat Dissipation. *Adv. Mater.* **2016**, *28* (7), 1413–1419.
- (18) Martinez, A. W.; Phillips, S. T.; Whitesides, G. M. Three-dimensional microfluidic devices fabricated in layered paper and tape. *Proc. Natl. Acad. Sci. U. S. A.* **2008**, *105* (50), 19606–19611.
- (19) Copic, D.; Park, S. J.; Tawfik, S.; De Volder, M. F.; Hart, A. J. Fabrication of high-aspect-ratio polymer microstructures and hierarchical textures using carbon nanotube composite master molds. *Lab Chip* **2011**, *11* (10), 1831–1837.
- (20) Mates, J. E.; Schutzius, T. M.; Qin, J.; Waldroup, D. E.; Megaridis, C. M. The Fluid Diode: Tunable Unidirectional Flow through Porous Substrates. *ACS Appl. Mater. Interfaces* **2014**, *6* (15), 12837–12843.
- (21) De Gennes, P.-G.; Brochard-Wyart, F.; Quéré, D. *Capillarity and Wetting Phenomena: Drops, Bubbles, Pearls, Waves*; Springer Science & Business Media, 2013.
- (22) Lobaton, E.; Salamon, T. Computation of constant mean curvature surfaces: Application to the gas–liquid interface of a pressurized fluid on a superhydrophobic surface. *J. Colloid Interface Sci.* **2007**, *314* (1), 184–198.
- (23) Nam, Y.; Sharratt, S.; Byon, C.; Kim, S. J.; Ju, Y. S. Fabrication and characterization of the capillary performance of superhydrophilic Cu micropost arrays. *J. Microelectromech. Syst.* **2010**, *19* (3), 581–588.
- (24) Mognetti, B. M.; Yeomans, J. Modeling receding contact lines on superhydrophobic surfaces. *Langmuir* **2010**, *26* (23), 18162–18168.
- (25) Byon, C.; Kim, S. J. Study on the capillary performance of micro-post wicks with non-homogeneous configurations. *Int. J. Heat Mass Transfer* **2014**, *68*, 415–421.
- (26) Ranjan, R.; Patel, A.; Garimella, S. V.; Murthy, J. Y. Wicking and thermal characteristics of micropillared structures for use in passive heat spreaders. *Int. J. Heat Mass Transfer* **2012**, *55* (4), 586–596.
- (27) Semperebon, C.; Forsberg, P.; Priest, C.; Brinkmann, M. Pinning and wicking in regular pillar arrays. *Soft Matter* **2014**, *10* (31), 5739–5748.
- (28) Ranjan, R.; Murthy, J. Y.; Garimella, S. V. Analysis of the wicking and thin-film evaporation characteristics of microstructures. *J. Heat Transfer* **2009**, *131* (10), 101001.
- (29) Moulinet, S.; Bartolo, D. Life and death of a fakir droplet: Impalement transitions on superhydrophobic surfaces. *Eur. Phys. J. E: Soft Matter Biol. Phys.* **2007**, *24* (3), 251–260.
- (30) Kusumaatmaja, H.; Blow, M.; Dupuis, A.; Yeomans, J. The collapse transition on superhydrophobic surfaces. *EPL (Europhysics Letters)* **2008**, *81* (3), 36003.
- (31) Whyman, G.; Bormashenko, E. How to make the Cassie wetting state stable? *Langmuir* **2011**, *27* (13), 8171–8176.
- (32) Ball, P. How wet can you get? *Nat. Phys.* **2016**, *12* (7), 718–718.
- (33) Shanahan, M. E. Capillary movement of nearly axisymmetric sessile drops. *J. Phys. D: Appl. Phys.* **1990**, *23* (3), 321.
- (34) Shanahan, M. A simple analysis of local wetting hysteresis on a Wilhelmy plate. *Surf. Interface Anal.* **1991**, *17* (7), 489–495.
- (35) Shanahan, M.; Di Meglio, J. Wetting hysteresis: effects due to shadowing. *J. Adhes. Sci. Technol.* **1994**, *8* (11), 1371–1380.
- (36) Woodward, J.; Gwin, H.; Schwartz, D. Contact angles on surfaces with mesoscopic chemical heterogeneity. *Langmuir* **2000**, *16* (6), 2957–2961.
- (37) Joanny, J.; De Gennes, P.-G. A model for contact angle hysteresis. *J. Chem. Phys.* **1984**, *81* (1), 552–562.
- (38) Yeo, J.; Choi, M. J.; Kim, D. S. Robust hydrophobic surfaces with various micropillar arrays. *J. Micromech. Microeng.* **2010**, *20* (2), 025028.
- (39) Kim, S. J.; Moon, M.-W.; Lee, K.-R.; Lee, D.-Y.; Chang, Y. S.; Kim, H.-y. Liquid spreading on superhydrophilic micropillar arrays. *J. Fluid Mech.* **2011**, *680*, 477–487.
- (40) Li, J.; Hou, Y.; Liu, Y.; Hao, C.; Li, M.; Chaudhury, M. K.; Yao, S.; Wang, Z. Directional transport of high-temperature Janus droplets mediated by structural topography. *Nat. Phys.* **2016**, *12*, 606–612.
- (41) Liu, Y.; Moevius, L.; Xu, X.; Qian, T.; Yeomans, J. M.; Wang, Z. Pancake bouncing on superhydrophobic surfaces. *Nat. Phys.* **2014**, *10* (7), 515–519.
- (42) Dhillon, N. S.; Buongiorno, J.; Varanasi, K. K. Critical heat flux maxima during boiling crisis on textured surfaces. *Nat. Commun.* **2015**, *6*, 8247.
- (43) Raj, R.; Adera, S.; Enright, R.; Wang, E. N. High-resolution liquid patterns via three-dimensional droplet shape control. *Nat. Commun.* **2014**, *5*, 4975.
- (44) Paxson, A. T.; Varanasi, K. K. Self-similarity of contact line depinning from textured surfaces. *Nat. Commun.* **2013**, *4*, 1492.
- (45) Do Carmo, M. P. *Differential Geometry of Curves and Surfaces*; Prentice-Hall: Englewood Cliffs, NJ, 1976; Vol. 2.
- (46) Ashcraft, C.; Grimes, R. G. In *SPOOLES: An Object-Oriented Sparse Matrix Library*; PPSC, 1999.
- (47) Brakke, K. A. *Surface Evolver Manual*; Mathematics Department, Susquehanna University: Selinsgrove, PA, 1994; 17870.
- (48) Papadopoulos, P.; Mammen, L.; Deng, X.; Vollmer, D.; Butt, H.-J. How superhydrophobicity breaks down. *Proc. Natl. Acad. Sci. U. S. A.* **2013**, *110* (9), 3254–3258.
- (49) Hansen, F.; Rodsrud, G. Surface tension by pendant drop: I. A fast standard instrument using computer image analysis. *J. Colloid Interface Sci.* **1991**, *141* (1), 1–9.
- (50) Hatano, Y.; Katsumura, Y.; Mozumder, A. *Charged Particle and Photon Interactions with Matter: Recent Advances, Applications, and Interfaces*; CRC Press, 2010.

(51) Preston, D. J.; Mafra, D. L.; Miljkovic, N.; Kong, J.; Wang, E. N. Scalable Graphene Coatings for Enhanced Condensation Heat Transfer. *Nano Lett.* **2015**, *15* (5), 2902–2909.

(52) Preston, D. J.; Miljkovic, N.; Sack, J.; Enright, R.; Queeney, J.; Wang, E. N. Effect of hydrocarbon adsorption on the wettability of rare earth oxide ceramics. *Appl. Phys. Lett.* **2014**, *105* (11601), 011601.

Supplementary Information

Coexistence of Pinning and Moving on a Contact Line

Zhengmao Lu^a, Daniel J. Preston^a, Dion S. Antao, Yangying Zhu, and Evelyn N. Wang^b

Department of Mechanical Engineering, Massachusetts Institute of Technology, Cambridge,
Massachusetts 02139, USA

I. Comparison Between Our Method and Surface Evolver

We compare results from our current method and the more commonly used Surface Evolver (SE) approach in Figure S1, using a unit cell from a square pattern array with cylindrical pillars as a benchmark case with $r = 1$, $L = 2.5$, $\theta_r = 30^\circ$, and $Bo \ll 1$. With our method, given a mean curvature κ , we solve for the capillary surface and calculate the liquid volume V in one unit cell. On the other hand, in SE, we choose a V , evolve the interface into a constant mean curvature surface, and evaluate κ as the Lagrange multiplier. Figure S1 gives V as a function of κ evaluated from both methods, showing excellent agreement.

Indeed, SE can handle a larger breadth of problems. Nevertheless, it is generally difficult to determine how close the surface is to the minimum energy configuration (the true solution) in SE, whereas it is easier to test the convergence and specify the relative error based on a certain mesh density using our current approach which relies on the finite element method to solve partial differential equations. Furthermore, to apply the capillary surface shape as the geometric constraint to the wicking or non-wetting applications, the interface shape has to be given as a function of pressure or κ . Following the previous approaches using SE with the volume constraint, one has to first solve for the dependence of the interface shape on the choice of V and then correlate V to κ ,

^a Zhengmao Lu and Daniel J. Preston contributed equally to this work

^b To whom correspondence should be addressed: enwang@mit.edu

which relates the shape to κ in an indirect manner. Meanwhile, the current approach directly gives the capillary surface shape as a function of κ , which facilitates integrating this method as a subroutine into modeling and optimization of geometric parameters for functioning of structured surfaces.

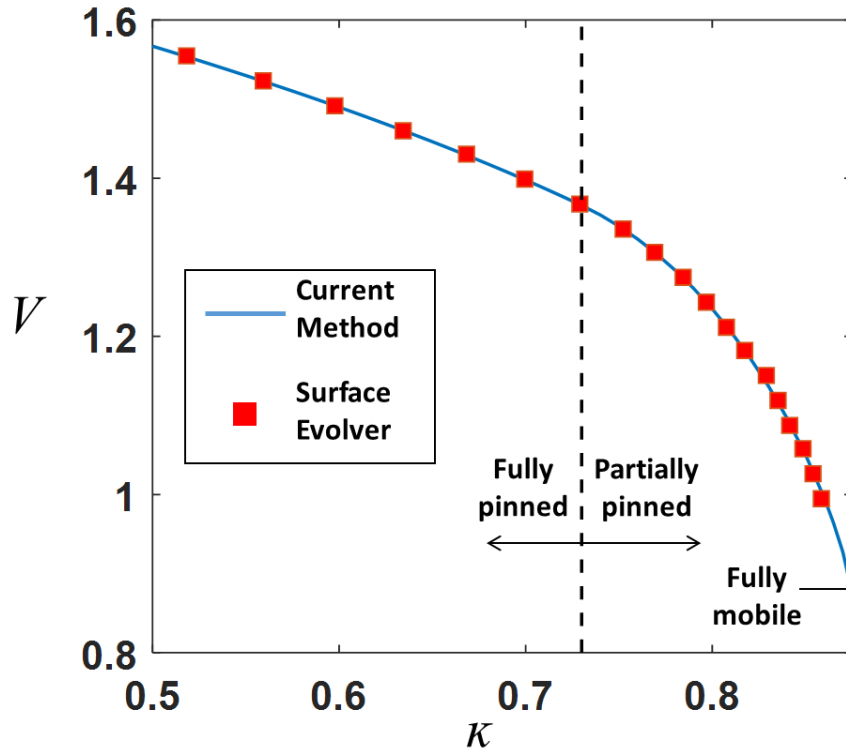


Figure S1. Volume V as a function of curvature κ evaluated using both our current method (solid blue line) and SE (solid red squares), which are in excellent agreement.

II. Implications of Capillary Surface Evolution

As κ varies, there are also changes in the lowest location on the interface (z_{min}) and the interface surface area normalized over its projection area (A^*) (Figure S2). When κ is small, the capillary surface is relatively flat, which makes A^* close to 1 and z_{min} close to 0. As κ increases, the interface extends into the unit cell, which causes the actual interface area to increase, i.e., $A^* > 1$, and the capillary surface to come closer to the bottom substrate (z_{min} decreases). In fluid repellency

applications, the pillar height needs to be greater than $|z_{min}|$ to maintain the Cassie-Baxter state. In the wicking process, a smaller z_{min} means larger flow resistance for liquid transport and A^* corresponds to the area for possible interfacial heat/mass transfer¹⁵. Hence, this work has important implications for superhydrophobic surfaces and fluidic-based thermal management applications which have not been well-captured in past work.

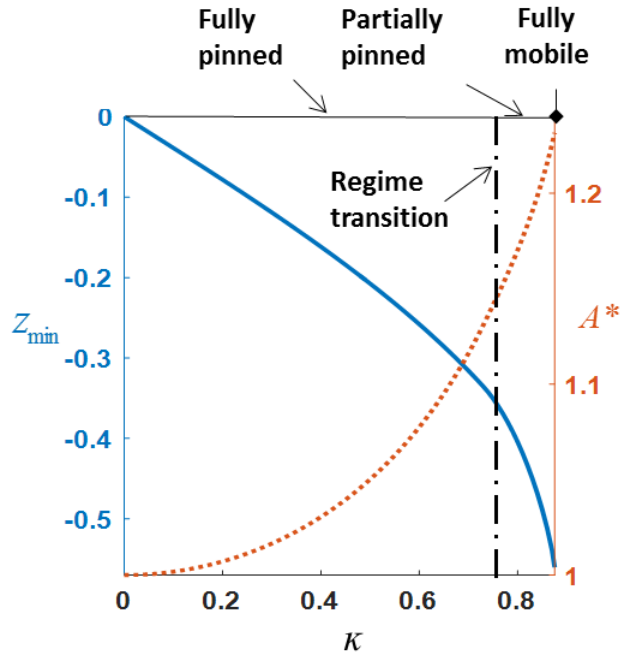


Figure S2. Lowest location on the interface z_{min} (blue solid line) and its normalized surface area A^* (orange dotted line) as a function of κ .

III. Image Processing for the Fully Mobile Contact Line

To verify the findings of our model, we created square patterned pillar arrays using nylon pillars with the water solution of Rhodamine B as the working fluid. Using a digital camera, we captured the fully mobile mode in Figure S3. To determine the exact contact line location, we first extracted the pillar edge coordinates (Curve 1 in Figure S3) in pixels and fit it with an ellipse. Since this ellipse is also the projection of the circular pillar cross-section, this gives us the camera tilting

angle $\alpha_c = \arccos (b/a)$, where a and b are the semi-major and semi-minor axes of the ellipse, respectively. The ellipse fitting also provides the x -coordinate of the center of the contact line x_0 . We then export the contact line coordinates (Curve 2 in Figure S3) in pixels. To compare Curve 2 to our model, the relative position in the x -direction has to be converted to that along the pillar circumference. The relative position in the y -direction is determined by the difference between Curve 1 and Curve 2, adjusted by α_c . Since the major axis of the ellipse is parallel to the camera projection plane, a also represents the undistorted pillar radius to which we normalize all of the dimensions.

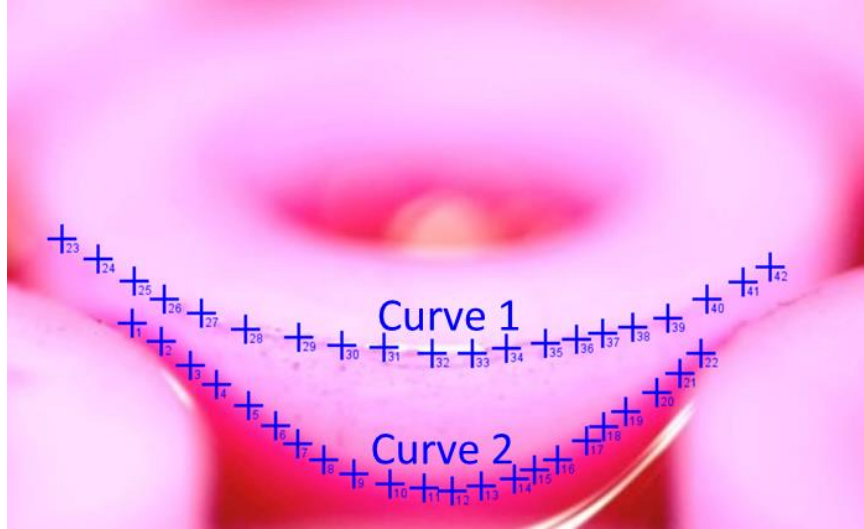


Figure S3. Image processing on the fully receding mode to extract the contact line location.

IV. Contact Line Receding in Silicon Micropillar Arrays

We experimentally observed all three regimes (Regime (I) fully pinned regime, Regime (II) partially pinned regime, and Regime (III) fully mobile regime) on microfabricated silicon pillar arrays (Figure S4 (a)) with an environmental scanning electron microscope (ESEM, EVO 50, Carl Zeiss). Imaging was performed with a 500 μm lower aperture to allow extended water vapor

pressure inside the chamber, and the backscatter detector was used to collect the image. The ESEM chamber was first purged with water vapor over five cycles to remove noncondensable gases. The pillars were then cooled to 2 °C on a Peltier stage inside the ESEM and water vapor was condensed on the pillars at 110% relative humidity until the sidewalls were completely wetted, corresponding to Regime (I) and shown in Figure S4 (b). The relative humidity was adjusted to 98% to promote evaporation of the water in order to observe the receding contact line behavior. Initially, the interface remained in Regime (I), but as evaporation continued and the volume of water present on the samples decreased, Regimes (II) and (III) were observed as the contact line receded down the pillar sidewall, shown in the time lapse in Figure S4 (c), where the location of the CL started to vary on the pillar surface.

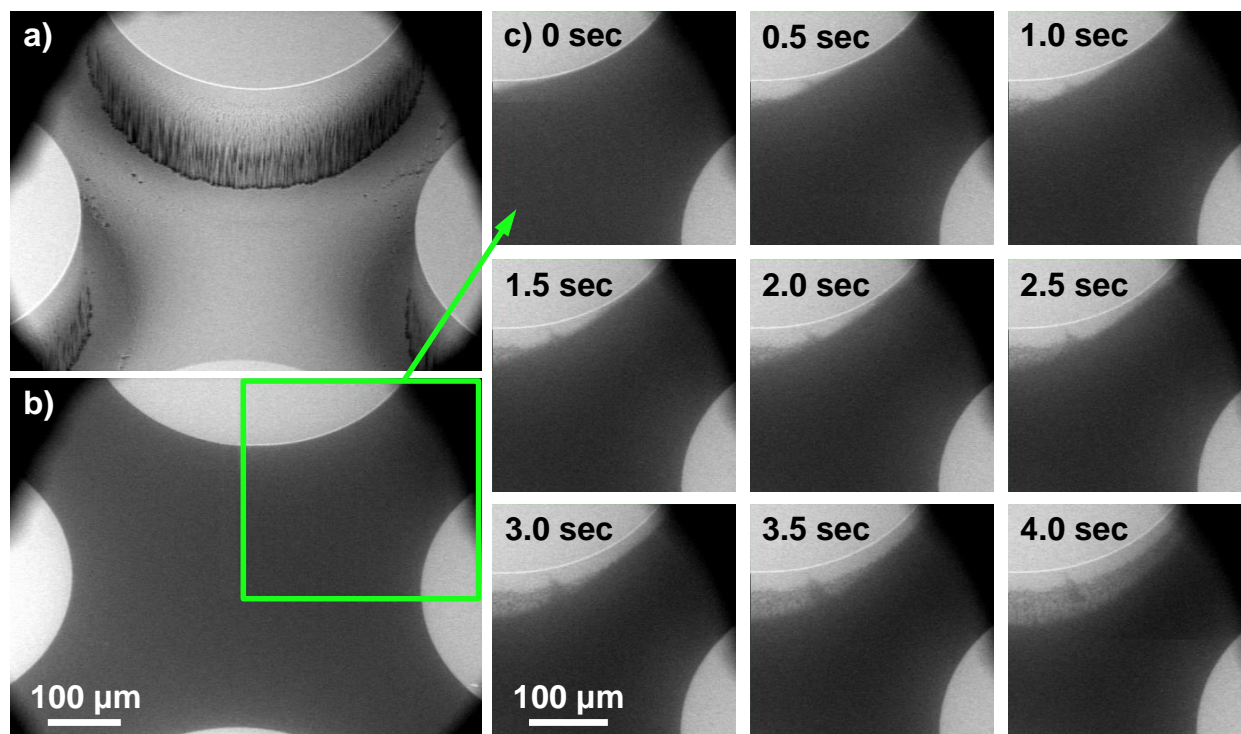


Figure S4. (a) Cylindrical silicon pillars were microfabricated for experimental imaging of the receding contact line with an environmental scanning electron microscope (ESEM). (b) The pillars were cooled and water vapor was condensed onto the pillars until their walls were completely wetted, corresponding to Regime (I). (c) This time lapse, zoomed into the sidewall of one pillar, shows the subsequent receding of the contact line during evaporation of liquid water; Regime (II) is present from 0 to 2.5 sec, after which Regime (III) is observed.

V. Capillary Surface in Square Cross-Section Micropillar Arrays

The current method can be easily extended to any micropillar array of constant cross-section. For example, Figure S5 (a) shows a unit cell of a square pattern micropillar array with pillars of square cross-section. The problem domain is constrained by symmetric boundaries and the CL. We plot the capillary surface in the fully receding regime for the case where the pillar side length $a_s = 1$ and $L = 2.5$ in terms of the 2-D contour solution in Figure S5 (b) and reconstruct the 3-D geometry in Figure S5 (c). In Figure S5 (c), the CL on square shape micropillars is not as smooth as the one on cylindrical micropillars due to the presence of a sharp corner which corresponds to a singularity in curvature. In reality, the micropillar corner can only contain a finite curvature, which would make the CL smoother.

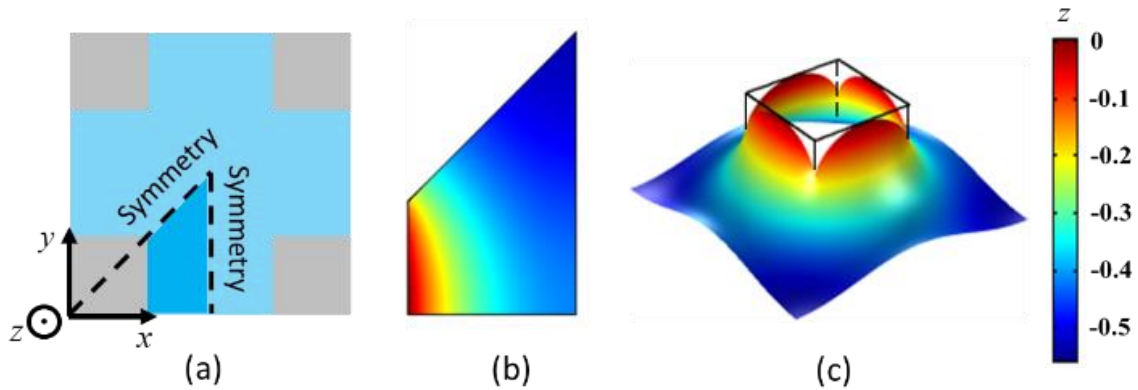


Figure S5 (a) Top view of a unit cell of a square pattern micropillar array with pillars of square cross-section. (b) 2-D contour map of the interface shape in the problem domain. (c) 3-D reconstruction of capillary surface around one pillar in a square pattern micropillar array with pillars of square cross-section.